The Effect of Surface Reconstruction on the Oxygen Reduction Reaction Properties of $LaMnO_3$

Reinis Ignatāns[1], Giuseppe Mallia[2], Ehsan A. Ahmad[2], Liam Spillane[3], Kelsey A. Stoerzinger[4], Yang Shao-Horn[5], Nicholas M. Harrison[2], and Vasiliki Tileli[1*]

[1]*Institute of Materials, École Polytechnique Fédéral de Lausanne, Station 12, 1015 Lausanne, Switzerland*

[2]*Department of Chemistry, Imperial College London, Exhibition Road, SW7 2AZ London, UK*

[3]*Gatan Inc., Pleasanton, CA 94588, USA*

[4]*School of Chemical, Biological, and Environmental Engineering, Oregon State University, Corvallis, OR 97331, USA*

[5]*Department of Materials Science and Engineering, Massachusetts Institute of Technology, Cambridge, MA 02139, USA*

E-mail: vasiliki.tileli@epfl.ch

Abstract

Perovskites have been widely studied for electrocatalysis due to the exceptional activity they exhibit for surface-mediated redox reactions. However, descriptors based on density theory calculations or experimental measurements have assumed a bulk-like configuration for the surfaces of these oxides. Herein, we probe the initial exposed surface and screened subsurface of as-grown $LaMnO_3$ particles, demonstrating that their augmented activity towards the oxygen reduction reaction (ORR) is related to a spontaneous surface reconstruction. Our approach involves high-energy resolution electron energy-loss spectroscopy (EELS) for fine structure probing of ionization edges under electron-beam conditions that leave the structure unaffected. To interpret the EELS results, we evaluate and compare with calculated spectra implementing several theoretical models. Simulation packages involving atomic multiplet theory, density functional theory using the muffin-tin approach, and electron hybrid density functional theory were used to quantitatively demonstrate that a La deficiency on the surface layers is responsible for equivalent tetrahedral Mn^{2+} sites on the reconstructed surface and, therefore, the +3 and +2 oxidation state of Mn coexist on the surface layers. This electronic and structural configuration of the as-synthesized particles is indirectly linked to strong adsorption pathways which promote the ORR on $LaMnO_3$ and thus it could prove to be valuable design feature in the engineering of catalytic surface

Introduction

Manganese oxides of the perovskite structure exhibit excellent catalytic activity towards the oxygen reduction reaction (ORR) in alkaline media[1,2] and are considered promising candidates to replace the costly noble metal catalysts for charge storage in electrochemical devices.[3–5] In particular, orthorhombic $LaMnO_3$ (LMO) particles are the leading ORR catalysts based on descriptors depicting activity as a function of e_g orbital filling.[6] This important finding by Suntivich *et al.* led to increased interest in perovskite oxide catalysts and extensive study of a number of perovskite structures using thin film growth techniques.[7,8] However, in most cases, perovksite nanoparticles have been found to outperform perovskite thin films in real electrochemical systems.[2] Their functionality is unambigiously linked to the surface character of the catalysts, however, the actual mechanism by which the reaction proceeds it not known yet. Most of the studies consider bulk-like structure for interpretation of the catalytic activity, however, studies also hinted to the role of possible surface reconstruction mechanisms[9] and surface chemical environment changes.[10] More recently, *in situ* and *operando* x-ray based studies have been implemented in order to acquire real-time information on the mechanism during ORR of maganeze oxides.[11] X-ray absorption spectroscopy (XAS) data showed that the Mn^{3+} environment of the bulk structure is critical for the high activity,[11] whereas studies on Mn spinel structures revealed that a mixed valence (between Mn^{3+} and Mn^{4+} or Mn^{2+} and Mn^{3+}) is the key to charge transfer from the catalyst to the adsorbed oxygen.[12] Apart from the valence, the Mn coordination has also been related to the activity.[12–14]

Herein, we report on the surface properties of as-synthesized $LaMnO_3$ particles by probing the surface and subsurface states by electron energy-loss spectroscopy (EELS). Similarly to XAS, EELS provides information on the energy dependence of the density of empty states in the conduction band (core-loss region)[15] but, unlike XAS, EELS in scanning transmission electron microscopy (STEM) mode is able to probe effects associated with the local environment of the surface regions. Electron probing of the Mn $L_{3,2}$ fine structure revealed a local

mixed valence on the first surface layers and this effect is correlates with changes on the shape of the O K edge pre-peak. Quantification of spectra containing all elements yielded a significant La-site deficiency at the surface. For the interpretation of the EEL spectra, detailed analysis using various theoretical models was performed. The density of states was computed using hybrid exchange density functional theory in an accurate local combination of atomic orbitals approximation. The resultant orbital decomposition was found to be consistent with an electrostatic picture of the bonding and thus interpretable within a simple point charge model and ligand field framework. In the distorted octahedral environment of the Mn ion in LMO the calculations suggest mixing of the $d_{x^2-y^2}$ and d_{z^2} orbitals. Population analysis of the charge density from the h-DFT calculations indicates the co-existance of Mn^{3+} and Mn^{2+} ions at the LMO surface.The influence of the charge state on the EELS spectra can be evaluated by computing the EEL spectra for various states and using them as standards for interpretation of the measured Mn $L_{3,2}$ fine structure, it is also possible to deduce that the surface layers are composed of reduced Mn ions sitting in La sites (Mn^{2+} in a 12-coordinated environment). This is further confirmed by the oxygen K edge fine structure where the loss of the pre-peak is a signature of the lack of hybridisation between the Mn and O orbitals. This further confirms the fact that part of the surface Mn^{2+} ions sit in the larger A site cage as opposed to the more confined B site octahedral configuration of the Mn^{3+} ion.

Methods

Sample preparation

$LaMnO_3$ single crystal particles were synthesised using the co-precipation method, as described before.[6] The same, working powders were used for which the catalytic activity was previously measured by Sintivich *et al.*[6] The size and shape of the particles varies dramatically and, as illustrated in Fig. 1, the surface of the particles shows atomic steps and is contamination-free. Direct interpretation of the images is hindered by the particle size (typ-

ically more that 100 nm up to 800 nm) and interference effects. For all S/TEM and EELS experiments, the particles were dispersed in liquid water to prevent any chance of chemical surface alteration with solvent solutions before analysis. Liquid suspended particles were then deposited onto commercially available lacey carbon support film mounted on copper grids. Spectrum imaging was performed on particle edges that were unsupported by the carbon film to ensure all data were pure LMO spectra with no carbon contribution from the support.

Transmission electron microscopy

Figure 1 shows a transmission electron micrograph taken on a spherical aberration (C_s) corrected at the image plane Thermofischer ScientificTitan 80-300 TEM operated at 300kV at a negative C_s of -13 μm and a defocus of 8 nm.

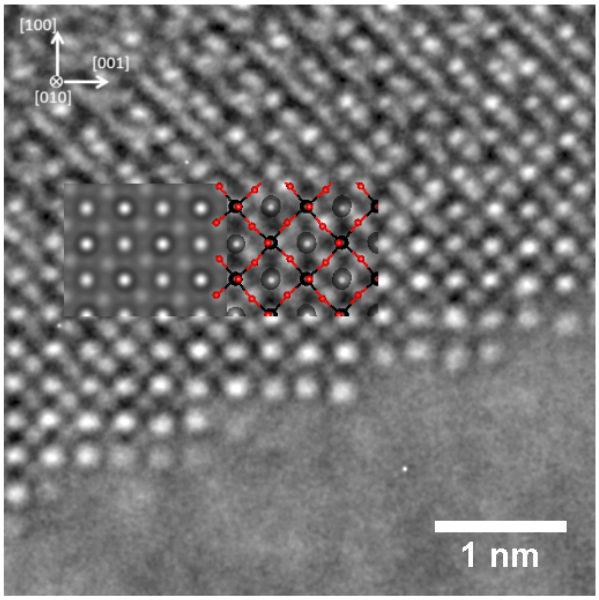


Figure 1: High-resolution TEM images of surface atomic layers of $LaMnO_3$ depicting the non-contaminated atomic step structure up to the very surface of the particle. The overlaid schematics depict the simulated HRTEM map along with simulations of the atomic positions where La is grey, Mn is black, and O is red.

Scanning transmission electron microscopy and electron energy loss spectroscopy

The scanning transmission electron microscopy studies were performed on a double spherical aberration (C_s) corrected Thermofischer Scientific Titan Themis 60-300 operated at 200 kV. All STEM EELS data acquisition was performed in spectrum imaging mode using a Gatan GIF Quantum electron energy-loss spectrometer and using the Gatan ADF STEM detector mounted in the GIF Quantum. The Themis electron monochromator was excited to give an energy resolution of 0.3 eV at spectrometer dispersion 0.1 eV/channel. All spectrum images were acquired using Gatan Digitalmicrograph at camera length 12.3 mm (in EFTEM mode), giving a convergence semiangle (alpha) of 28 mrad, collection semiangle (beta) of 47.3 mrad and ADF inner detection angle of 98.5 mrad. All spectrum imaging was performed in dual EELS mode with the low loss energy offset set to 0 eV to allow for post acquisition energy scale correction. The high loss energy offset was adjusted so that the oxygen K, manganese $L_{3,2}$ and/or lanthanum $M_{5,4}$ edges were in the field of the view of the Quantum camera. Data were acquired at 0.1 eV/channel for fine structural analysis and 0.25 eV/channel for quantification. Probe current of approximately 100 pA was chosen to maximise the EELS signal and to limit the electron beam induced damage. No damage or contamination were seen after acquisition. All data processing was performed using Gatan Digitalmicrograph v. 3.4. Energy drift was removed from all core loss spectrum image data sets by using the "align SI by peak" function applied to the sibling low loss spectrum image. Quantification was performed using the multiple linear least squares (MLLS) based quantification routine using quantification parameters shown in Table 1. These parameters were previously optimised for stoichiometric LMO. All ionisation edges were specified as non-overlapping and the ELNES contribution (as shown in Table 1) was excluded from the quantification calculation. Plural scattering was included in the quantification calculations allowing composition result to be normalised for changes in specimen thickness. Atomic multiplet simulations for the Mn $L_{3,2}$ white lines were performed using CTM4XAS for: Mn^{3+} in D_{4h} symmetry crystal field

and Mn^{2+} in T_d and O_h symmetries. The results of these calculations were imported into Digitalmicrograph and were used as fit components in a MLLS fit to background subtracted Mn $L_{3,2}$ edges present in spectrum images acquired from the LMO particles. 2D maps of the fit coefficients were then generated in order to map out local changes in Mn valence and coordination.

Table 1: EELS Quantification Parameters Applied

Element	Fit Range (eV)	ELNES Width (eV)	Signal Sum Width (eV)
O	460.8 | 602.0	20.0	50
Mn	603.0 | 721.0	31.0	50
La	713.0 | 951.5	69.5	50

Computational Details

The calculations of the Mn $L_{3,2}$-edge and the O K-edge ELNES were performed by FDMNES code with the full-multiple-scattering approach.[16] Anti-ferromagnetic orthorhombic perovskite oxide structure (space group number 62 in the *Pbnm* setting), with the lattice parameters a = 5.5367 Å, b = 5.7473 Å and c = 7.6929 Å, was used for the $LaMnO_3$ spectral calculations.[17–19] Self-consistent spin polarized electronic structure calculation within FDMNES was performed after which spectrum calculation was done. Hubbard value U = 4 eV was used for better treatment of the Mn $3d$ orbitals.[20] Cluster radius of 7 Å surrounding the absorbing atom was found to be sufficient for a converged calculated spectrum. Calculated spectra were convoluted with the arctangent core-hole broadening model within FDMNES with $\Gamma_{\text{Hole}} = 0.34$ eV and $\Gamma_{\text{Hole}} = 0.20$ eV values (which are calculated automatically) for the manganese $L_{3,2}$ and oxygen K edges respectively.

Additionally, $L_{3,2}$ edge of the Mn atom at various oxidation states and crystal fields was calculated by the CTM4XAS 5.5 code.[21] For the Mn^{3+} in the D_{4h} symmetry (approximating manganese in the bulk of the $LaMnO_3$), crystal field parameters 10Dq = 1.5 eV, Ds = 0.4 eV

and Dt = 0.05 eV were chosen following Castleton and Altarelli.[22] Lorentzian (0.2 eV) and Gaussian (0.7 eV) broadening was applied to calculated spectra to match the experimental Mn $L_{3,2}$ line-shape. Additional spectral calculations of the Mn^{2+} ions in the O_h and T_d crystal fields with the 10Dq values of 1.5 eV and 0.5 eV respectively were performed. Comparably small crystal field splitting value in the Td symmetry is used by following previous results.[23] The same broadening parameters as found in the bulk of the material are applied to the calculated spectra of the Mn^{2+}, therefore giving reasonable expected line-shape.

DFT calculations have been performed using the CRYSTAL17[24] software package, based on the expansion of the crystalline orbitals as a linear combination of a local basis set (BS) consisting of atom centred Gaussian orbitals. The Mn and O atoms are described by a triple valence all-electron BS: an 86-411d(41) contraction (one s, four sp, and two d shells) and an 8-411d(1) contraction (one s, three sp, and one d shells), respectively; the most diffuse sp(d) exponents are α^{Mn}=0.4986(0.249) and α^{O}= 0.1843(0.6) Bohr^{-2}.[25] The La basis set includes a nonrelativistic pseudopotential to describe the core electrons, while the valence part consists of a 411p(411)d(311) contraction scheme with three s, three p and three d shells). The most diffuse exponent is α^{La}=0.15 Borh^{-2} for each s,p and d.[26] Electron exchange and correlation are approximated using the B3LYP hybrid exchange functional.[27–29]

Results and Discussion

$LaMnO_3$ (LMO) exhibits a Jahn-Teller (J-T) distorted orthorhombic *Pnma*) crystal structure at room temperature with distorted MnO_6 octahedra (point group D_{2h}) at trivalent Mn^{3+} site ($3d^4$ electron configuration). The h-DFT calculations reproduce this strong orbital interaction with the lattice and thus the symmetry breaking distortion. The computed electronic structure of the Mn^{3+} d^4 electrons in the LMO results in a distorted oxygen octahedron along one axis (Fig. 2(b)). This distortion along the z axis (Jahn-Teller distortion) breaks the local symmetry lifting the degeneracy of the highest energy occupied electronic

state of the e_g orbitals (as compared to the non-distorted environment as seen in Fig. 2(a)) giving a distinct ground state for the energetically highest electron. Within this electronic picture, the half-filled e_g has been assumed to play a defining role in the catalytic properties for the ORR of this oxide compared with other transition metal perovskites.[6] However, the MnO_6 octahedron is not distorted only along one axis in the LMO, the distortions occur along two axis giving rise to three different Mn-O bond lengths and local symmetry lowering to D_{2h}. Calculations of the energy levels for the spin up case (the spin down case is equivalent and is not shown for clarity) as a function of increased deformation of the MnO_6 octahedron are shown in Fig. 2, along with the corresponding atomic models. The Fermi level is also indicated for reference. In the case of a symmetrical oxygen octahedron (point group O_h) shown in Fig. 2(a), the energy levels are split into two states. The $d_{x^2-y^2}$ and d_{z^2} (e_g orbitals) are found to be degenerate, but when a distortion along the z axis is included the e_g orbitals split as shown in Fig. 2(b). This geometry corresponds to the D_{4h} symmetry, which is typically assumed to represent the octahedra configuration in LMO. In reality, the environment around the Mn^{3+} ion is less symmetric with the point group D_{2h} as seen in Fig. 2(c). Additional distortion in the xy plane within octahedra leads to a complete separation of the filled t_{2g} states and the mixing of the $d_{x^2-y^2}$ and d_{z^2} orbitals ($d_{x^2-y^2}$ wavefunction acquires some nature of the d_{z^2} and vice versa (see Supplemental Information for more details). This mixing of the d energy levels (one filled, one empty) on an atomic level could be a contributor to the enhancement of the ORR activity for LMO.[30]

A local, direct method for experimentally determining the empty density of states is electron energy-loss spectroscopy in a transmission electron microscope. Advances in the instrumentation in recent years have made it possible to perform experiments with both high energy and spatial resolution. The information of the fine structure gained from core-loss edges can provide direct evidence of the hybridisation of oxygen $2p$ and manganese $3d$ states when comparing the surface to the bulk of the LMO crystal. The treated data of the spectrum image (Fig. 3(b)) for oxygen K and Mn $L_{3,2}$ after removal of background and

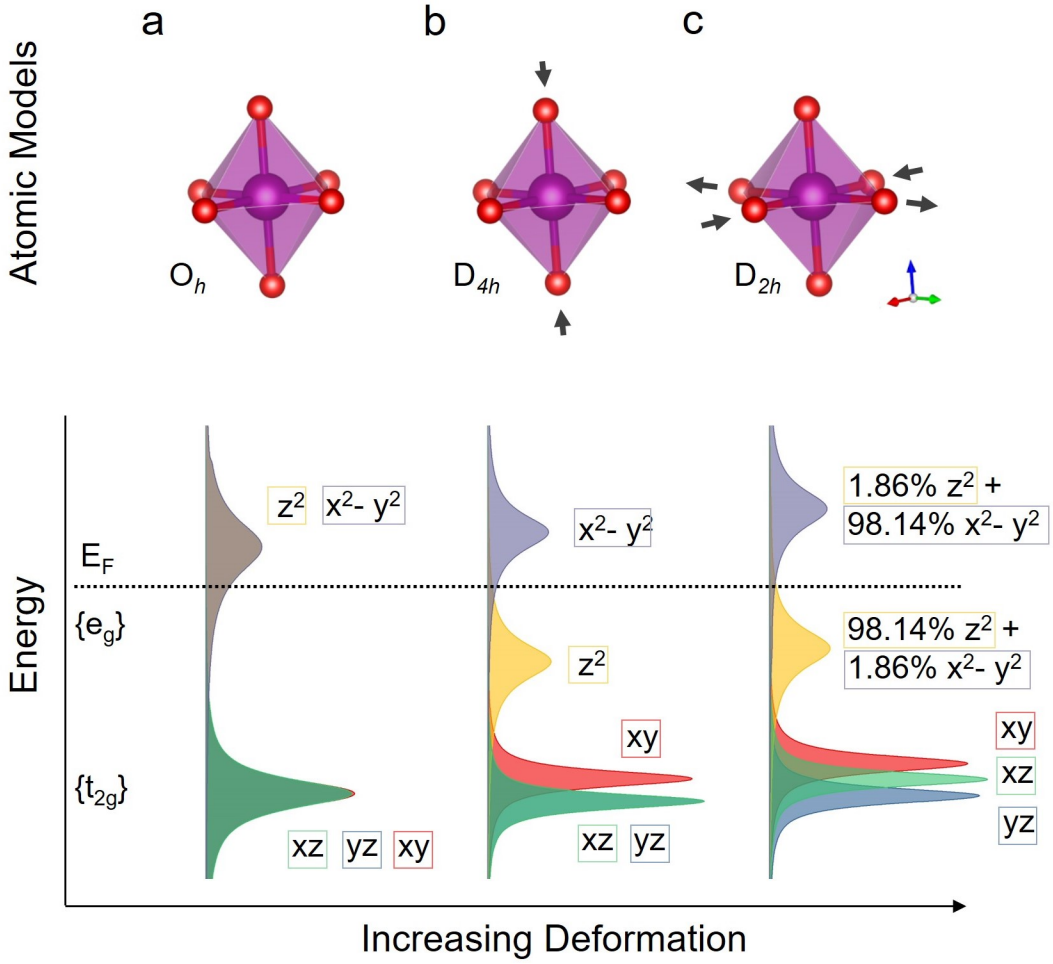


Figure 2: Atomic models and corresponding calculated density of states for an isolated MnO_6 octahedron as a function of increasing deformation. Shown are the results for the simplified symmetric case O_h (a), the asymmetric one-axis case D_{4h} (b), which is normally used to model LMO, and the two-axis asymmetry D_{2h} (c), which represents the Jahn-Teller distorted LMO.

thickness effects are shown in Fig. 3(a); the La $M_{5,4}$ edge is omitted as there is no change of its fine structure. The near-edge fine structure (ELNES) of the Mn L_3 reveals a shift towards lower energies accompanied with a minimisation of the oxygen pre-peak (α) evident in the first surface layers of the particle. The shift of the surface Mn (from γ to β as indicated in Fig. 3(a)) is about $\sim$ 1.5 eV to lower energy. This along with the L_2/L_3 intensity ratio change can be readily attributed to the change in the valence, i.e. the manganese is reduced to the +2 oxidation state at the surface.[31]

To better understand the distribution of elements at the surface and the bulk of the as-synthesised LMO, quantification of the EEL spectrum image, that also includes the La peak, was performed. The results, shown in Fig. 3(c), confirm the bulk structure with the nominal composition of 20:20:60 for La:Mn:O. Near the surface however, a deficiency in La is evident, whereas Mn remains relatively stable. The deficiency of La sites on surfaces of LMO films was previously reported by resonant inelastic x-ray spectroscopy measurements on thin films.[32] This deficiency can be accounted for by the loss of oxidation of Mn, meaning that it tends to hop to the La site, possibly occupying both Mn and La sites on the surface of the perovskite. Indeed, possible occupation of the Mn in La vacancies would reduce the valence of Mn. Relative to the electrocatalytic activity of LMO, it is was previously reported that the La bridge sites can interfere with the adsorption of O on Mn sites.[33] Replacement of La by Mn^{2+} is thus likely to result in an increase in the overall catalytic activity by means of increased presence of Mn ions at the surface and subsurface. In addition, tuning the La-site deficiency can affect the oxygen vacancies and the valence of the B-site can result in an overall enhancement of the activity.[34] At the same time, previous DFT calculations[35] predicted that the reduced valence of the Mn ions can favour the binding of *OOH, one of the steps involved in the pathway of electrocatalytic oxygen reduction.

Figure 4 compares the experimental bulk-like (subsurface) and surface Mn $L_{3,2}$ edges with selected theoretically calculated spectra. The calculations for the bulk Mn^{3+} include three approaches; the open access CTM4XAS program that is based on atomic multiplet theory,

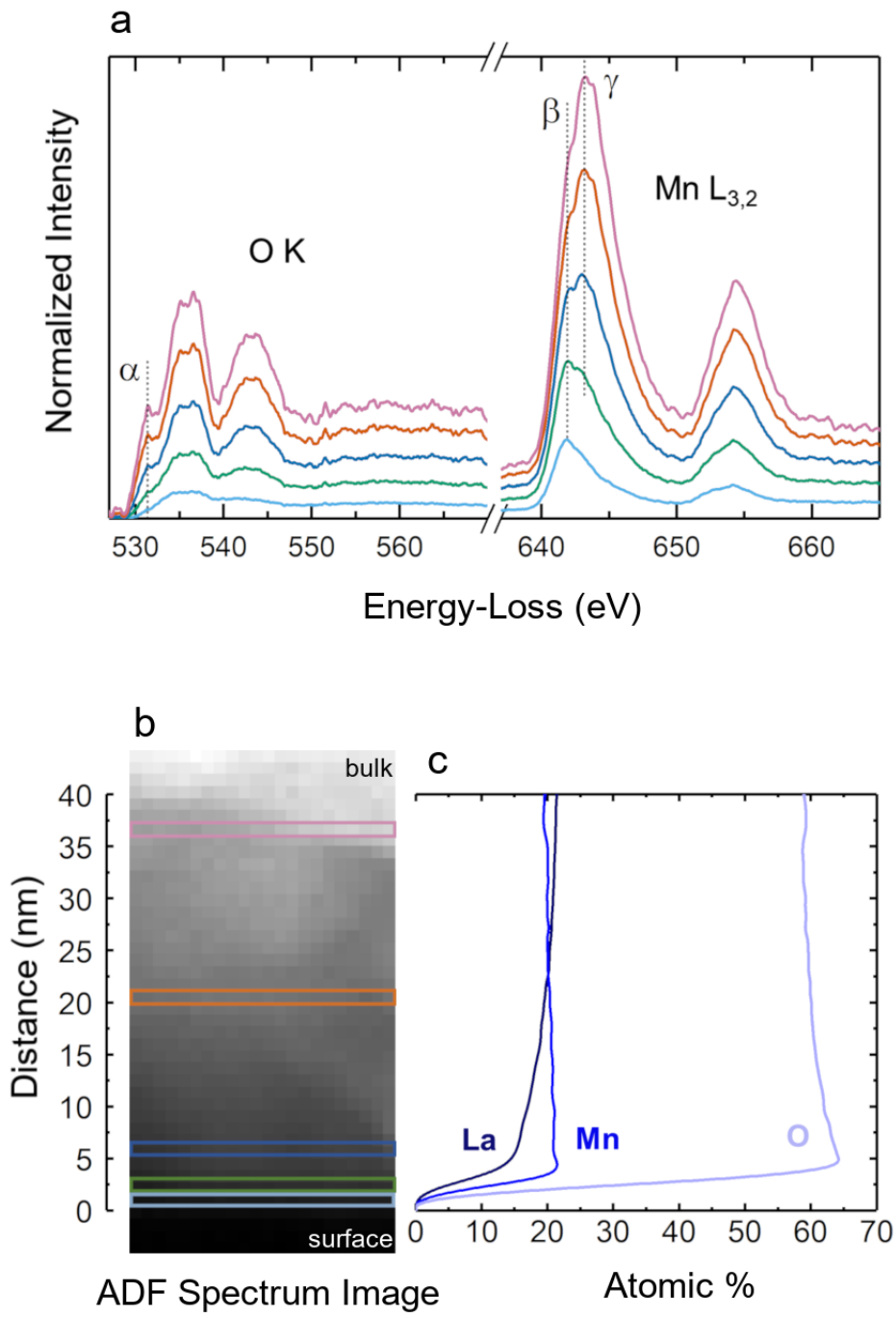


Figure 3: (a) Electron energy-loss spectra showing the fine structure of the oxygen K and Mn $L_{3,2}$ edges (SI3) from the surface (light blue) to the bulk (magenta). (b) Annular dark field (ADF) image showing the probed area with annotated regions of the spectra in (a), and (c) quantification of the EEL spectra showing the relative composition of all three elements present, La, Mn, and O, as a function of distance from the surface (0 nm) to the bulk (20 nm and above).

the open-access FDMNES program that is based on density functional theory calculations using the muffin-tin approach, and the CRYSTAL program that is based on an electron hybrid density functional theory (for more details see Methodology in Supplemental Information). The latter can only calculate the manganese L_3 edge since spin orbit splitting is not accounted for, instead the single DOS of the unoccupied $2p$ to $3d$ states is produced. For the bulk case, Figure 4(a), the all electron and muffin-tin based DFT and the simple electrostatic model all produce a similar description of the electronic structure which is consistent with that measured. The trend reveals, as reported previously for Mn-based +3 oxides,[31] that the main L_3 peak is broad and centred at 642 eV. Its fine structure exhibits features on the higher energy side of the main peak with the main contribution coming from the J-T splitting of the e_g orbitals in the D_{2h} or D_{4h} symmetry. For the case of the surface, Figure 4(b), several calculated spectra were used to interpret the results. Atomic multiplet calculations in various crystal fields were performed for Mn^{2+} octahedral and tetrahedral coordinations, whereas compounds showing these two geometries were used to calculate DFT-based spectra. In $MnFe_2O_4$ the Mn is at the +2 oxidation state with tetrahedral coordination whereas in MnO Mn^{2+} is found in an octahedral coordination. The position of the peak is well confirmed as the +2 oxidation state for all cases. However, discrepancies in the fine structure of the octahedral vs tetrahedral coordinations arise. Specifically, both calculations agree that the difference between the two coordinations has to do with features in the fine structure located at low energy for the tetrahedral case whereas the features location for the octahedral coordination is after the main peak. The pre L_3 peak is related to transitions of orbitals with t_{2g} character and it is typically associated with the 6-fold coordination of the octahedral configuration.

Relating these contributions from bulk to surface to the experimental EELS data, multiple linear least squares (MLLS) fitting was performed. Having established the conformal calculated spectra under the different theoretical approaches, the CTM4XAS spectra were chosen for the fit. Figure 5 indicates the maps of the fitted spectrum image (a) to the Mn^{3+}

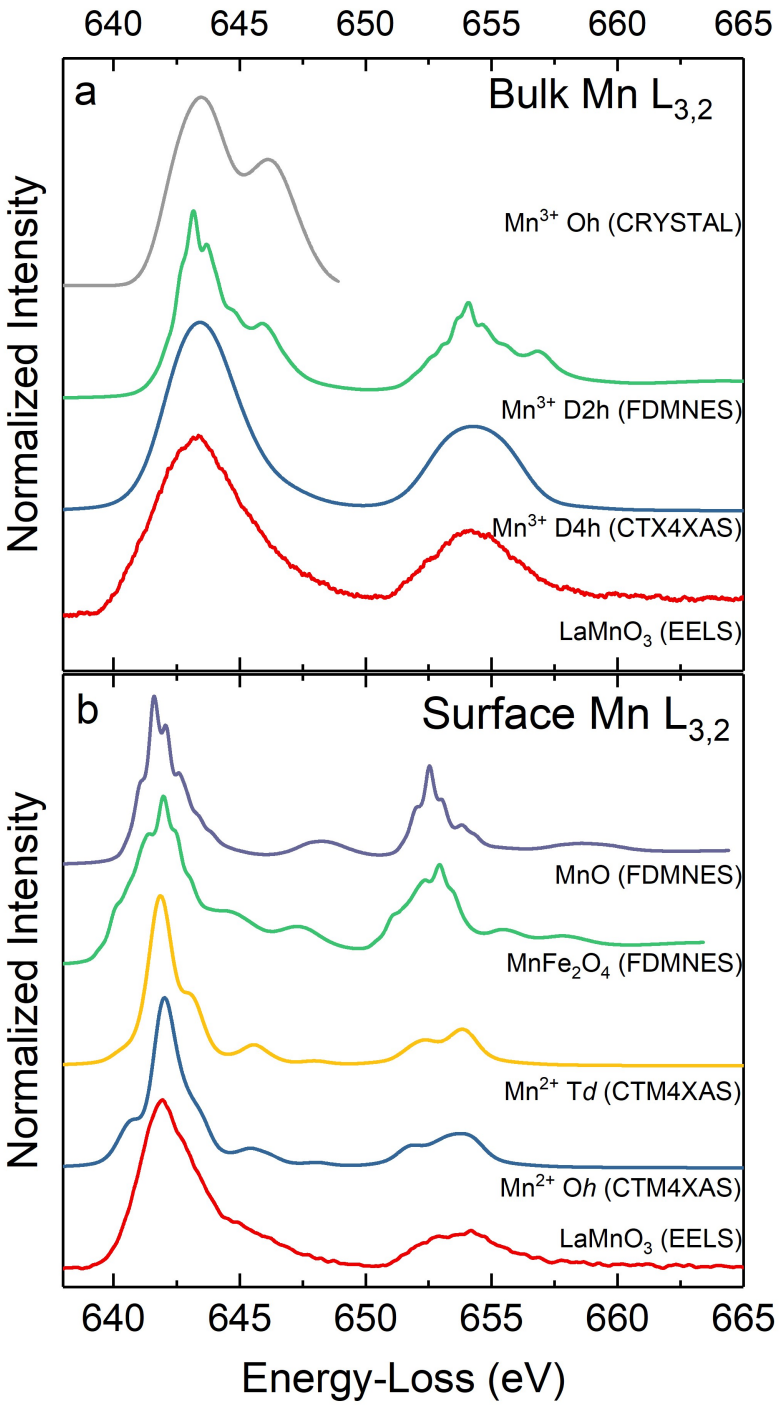


Figure 4: Theoretical calculations for the J-T distorted LMO crystal taking account octahedra distortion, valence and coordination for the bulk (a) and the surface (b) of the experimental Mn $L_{3,2}$ ELNES. The spectra have been aligned with respect to the main L_3 peak and ordered according to the complexity of the calculated spectra.

D_{4h} (b), the Mn^{2+} T_d (c), and the Mn^{2+} O_h (d). A comparison of the relative intensities of the three contributions is shown in 5(e). As expected, the D_{4h} Mn^{3+} signal dominates the bulk. At the first few layers of the surface however (close to 0 nm distance), the character changes dramatically and the maps reveal a significant contribution of T_d Mn^{2+} whereas for the O_h Mn^{2+} the fit is within the noise. The T_d Mn^{2+} character fits well with the surface La deficiency, further implying that the Mn ions on the surface occupy 12-coordinated La sites. The resulting $3d$ orbital splitting in a 12-coordinated cubo-octahedral site is equivalent to a weak crystal field with the T_d symmetry. To deduct the equivalence of the tetrahedral (T_d) and 12-coordinated cubo-octahedral sites we use the point charge model (See Supporting Information) to calculate the energy level splitting as a function of M-O distance, Fig. 6. 12-coordinated and T_d sites produce reversed orbital splitting pattern similar to the one in O_h symmetry. However, the change alone of the Mn site symmetry from the O_h to the 12-coordinated one (while preserving the Mn-O distances), would already reduce the t_{2g}-e_g splitting by two. Considering that the average bond length in the La site is about 1.4 times larger than in the normal Mn site, the t_{2g} to e_g splitting is reduced even further due to the decreased crystal field, Fig. 6. Overall, the energetical splitting of the t_{2g} and e_g orbitals for the manganese residing in the perovskite A site is expected to be roughly 20% of the magnitude when the manganese is in the B site. Therefore, the increased distance of the oxygen neighbours on the A site of the perovskite explains well the much weaker hybridisation of the Mn^{2+} with the oxygen on the surface (loss of pre-peak at the surface).

Evidence of this transformation is also confirmed by the projected density of states of the Mn and La orbitals and their comparison with the oxygen K edge. Figure 7 shows the EEL spectra of the oxygen K edge for the surface and the bulk overlapped with the calculated spectrum using FDMNES. Also shown are the calculated projected density of states for all the manganese and lanthanum orbitals (filled curves). The O K edge can therefore be interpreted within three distinct regions. Firstly, the calculations show strong hybridisation of the O $2p$ and Mn $3d$ depicted in the pre-peak of the edge (corresponding to the one free spin

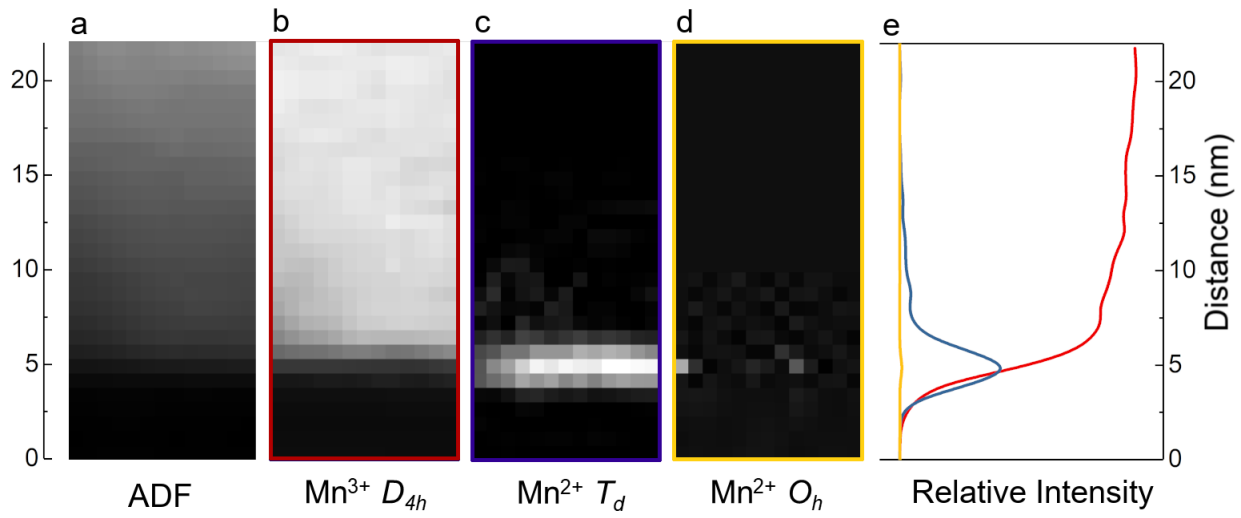


Figure 5: MLLS maps of EELS spectrum image (a) fitted for Mn L_3 edge based on CTM4XAS calculated spectra for the D_{4h} Mn^{3+} (b), the T_d Mn^{2+} (c), and the O_h Mn^{2+} (d). Also shown is the relative contribution of the three profiles (e).

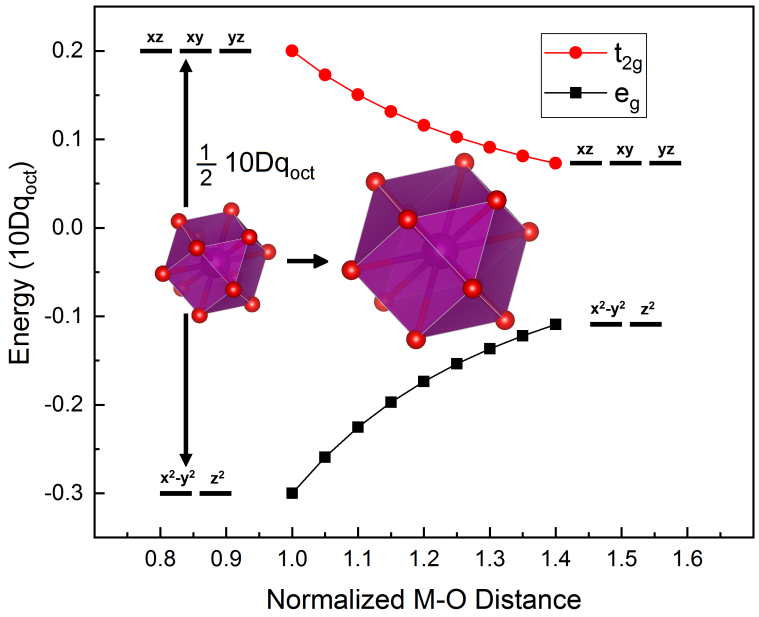


Figure 6: Calculated $3d$ orbital ordering diagram in a 12-coordinated cubo-octahedral site. Metal - oxygen distance is normalized to the average bond length of the B site. Value of 1.4 corresponds to the average bond length in the LMO A site. Energy is scaled to the 10Dq (crystal field splitting) value of octahedral site with normalized M-O distance of the value one. As it can be seen, when increasing the metal-oxygen bond length, the magnitude of splitting is reducing.

up state and completely free spin down states of the manganese). A region corresponding to the La orbitals (between 4 - 10 eV) follows and the last broad peak around 13 eV exhibits predominately Mn 4*sp* character. The calculations accurately predict the oxygen K edge for $LaMnO_3$ and the assignment of the features seen in the oxygen K edge is very similar to previously reported configuration interaction calculations.[36]

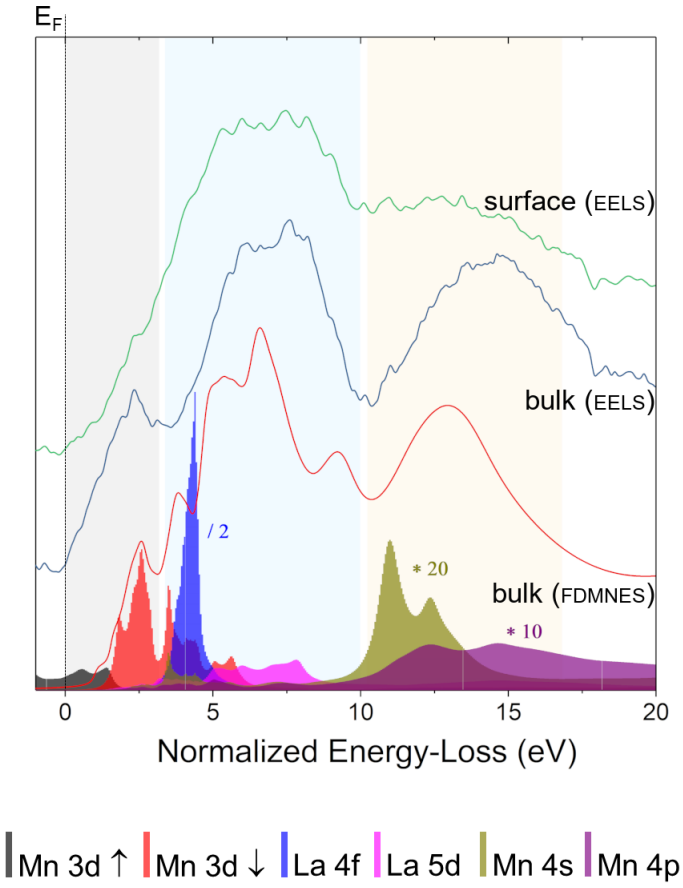


Figure 7: Projected density of states of the Mn 3*d* (spin up and spin down), Mn *sp*, La 4*f*, and La 5*d* (spin up and spin down configurations are equivalent and therefore only spin down is shown for clarity) as calculated from FDMNES. Shown is also the total FDMNES calculated EEL spectrum for the oxygen K edge along with the experimental EEL spectra for the bulk and the surface. The energy scale was shifted to zero on the onset of the edge, being also the onset of the Fermi level for the projected density of states.

Conclusion

Based on the chemical profile of the surface and subsurface of $LaMnO_3$ electrocatalytic particles, three complementary mechanisms could be responsible for the enhanced oxygen reduction reaction activity. Starting from the bulk, this slight mixing of the orbitals in the octahedra of the J-T distorted structure could make all possible absorption sites behave the same, independent of their electron density surrounding them. On the surface, the reduction of the oxidation state of Mn in relation to the La-site deficiency is linked to its partial substitution with Mn in a +2 oxidation state that are no longer hybridised with surrounding oxygen ions. Possibility of hydroxide groups terminating the surface layers is not excluded, however these species are not probed by EELS and therefore their contribution has been omitted. Despite the likely presence of hydroxides, the evidenced surface configuration exposes the Mn^{2+} ions occupying the A bridge sites and further favours the oxygen absorption by the A bridge sites. The coexistence of Mn^{2+} with Mn^{3+} sites has been shown to occur during ORR[12] and therefore this double ionic valence of the transition metal could be linked to a more efficient pathway that promotes the ORR activity of LMO particles.

Acknowledgement

This work was supported by the Swiss National Science Foundation (SNSF) under award number 200021_175711. Fruitful discussions on DFT modelling with Dr. Ross Webster are acknowledged. The authors thank Dr. Martial Duchamp and Prof. Rafal E. Dunin-Borkowski for assistance with initial experiments at Ernst-Ruska Centre at Julich and Dr. Anna Carlsson from ThermoFisher Scientific for support on optimisation of microscope operating conditions.

Supporting Information Available

The following files are available free of charge.

- Supporting Information: It includes details of the crystal field splitting diagram formation.

References

(1) Stoerzinger, K. A.; Risch, M.; Han, B.; Shao-Horn, Y. Recent Insights into Manganese Oxides in Catalyzing Oxygen Reduction Kinetics. *ACS Catal.* **2015**, *5*, 6021–6031.

(2) Marcel Risch, Perovskite Electrocatalysts for the Oxygen Reduction Reaction in Alkaline Media. *Catalysts* **2017**, *7*, 154.

(3) Thackeray, M. M. Manganese Oxides for Lithium Batteries. *Prog. Solid State Chem.* **1997**, *25*, 1–71.

(4) Winter, M.; Brodd, R. J. What are Batteries, Fuel Cells, and Supercapacitors? *Chem. Rev.* **2004**, *104*, 4245–4270.

(5) Simon, P.; Gogotsi, Y. Materials for Electrochemical Capacitors. *Nat. Mater.* **2008**, *7*, 845–854.

(6) Suntivich, J.; Gasteiger, H. A.; Yabuuchi, N.; Nakanishi, H.; Goodenough, J. B.; Shao-Horn, Y. Design Principles for Oxygen-Reduction Activity on Perovskite Oxide Catalysts for Fuel Cells and Metal-Air Batteries. *Nat. Chem.* **2011**, *3*, 546–550.

(7) Stoerzinger, K. A.; Lü, W.; Li, C.; Ariando,; Venkatesan, T.; Shao-Horn, Y. Highly Active Epitaxial $La_{(1-x)}Sr_xMnO_3$ Surfaces for the Oxygen Reduction Reaction: Role of Charge Transfer. *J. Phys. Chem. Lett.* **2015**, *6*, 1435–1440.

(8) Eom, C. J.; Kuo, D.-Y.; Adamo, C.; Moon, E. J.; May, S. J.; Crumlin, E. J.; Schlom, D. G.; Suntivich, J. Tailoring Manganese Oxide with Atomic Precision to Increase Surface Site Availability for Oxygen Reduction Catalysis. *Nat. Commun.* **2018**, *9*, 4034.

(9) Lin, Y.; Wen, J.; Hu, L.; Kennedy, R. M.; Stair, P. C.; Poeppelmeier, K. R.; Marks, L. D. Synthesis-Dependent Atomic Surface Structures of Oxide Nanoparticles. *Phys. Rev. Lett.* **2013**, *111*, 156101.

(10) Sanchez-Santolino, G.; Tornos, J.; Bruno, F.; Cuellar, F.; Leon, C.; Santamara, J.; Pennycook, S.; Varela, M. Characterization of Surface Metallic States in $SrTiO_3$ by Means of Aberration Corrected Electron Microscopy. *Ultramicroscopy* **2013**, *127*, 109 – 113.

(11) Stoerzinger, K. A.; Risch, M.; Suntivich, J.; Lü, W. M.; Zhou, J.; Biegalski, M. D.; Christen, H. M.; Ariando,; Venkatesan, T.; Shao-Horn, Y. Oxygen Electrocatalysis on (001)-Oriented Manganese Perovskite Films: Mn Valency and Charge Transfer at the Nanoscale. *Energy & Environ. Sci.* **2013**, *6*, 1582.

(12) Risch, M.; Stoerzinger, K. A.; Han, B.; Regier, T. Z.; Peak, D.; Sayed, S. Y.; Wei, C.; Xu, Z.; Shao-Horn, Y. Redox Processes of Manganese Oxide in Catalyzing Oxygen Evolution and Reduction: An in Situ Soft X-ray Absorption Spectroscopy Study. *J. Phys. Chem. C* **2017**, *121*, 17682–17692.

(13) Lima, F. H. B.; Calegaro, M. L.; Ticianelli, E. A. Investigations of the Catalytic Properties of Manganese Oxides for the Oxygen Reduction Reaction in Alkaline Media. *J. Electroanal. Chem.* **2006**, *590*, 152–160.

(14) Lima, F. H. B.; Calegaro, M. L.; Ticianelli, E. A. Electrocatalytic Activity of Manganese Oxides Prepared by Thermal Decomposition for Oxygen Reduction. *Electrochim. Acta* **2007**, *52*, 3732–3738.

(15) Egerton, R. F. Electron Energy-Loss Spectroscopy in the TEM. *Rep. Prog. Phys.* **2008**, *72*, 016502.

(16) Guda, S. A.; Guda, A. A.; Soldatov, M. A.; Lomachenko, K. A.; Bugaev, A. L.; Lamberti, C.; Gawelda, W.; Bressler, C.; Smolentsev, G.; Soldatov, A. V.; Joly, Y. Optimized Finite Difference Method for the Full-Potential XANES Simulations: Application to Molecular Adsorption Geometries in MOFs and Metal–Ligand Intersystem Crossing Transients. *J. Chem. Theory Comput.* **2015**, *11*, 4512–4521.

(17) Grazulis, S.; Daskevic, A.; Merkys, A.; Chateigner, D.; Lutterotti, L.; Quiros, M.; Serebryanaya, N. R.; Moeck, P.; Downs, R. T.; Le Bail, A. Crystallography Open Database (COD): an open-access collection of crystal structures and platform for world-wide collaboration. *Nucleic Acids Res.* **2012**, *40*, D420–D427.

(18) Rodríguez-Carvajal, J.; Hennion, M.; Moussa, F.; Moudden, A. H.; Pinsard, L.; Revcolevschi, A. Neutron-Diffraction Study of the Jahn-Teller Transition in Stoichiometric $LaMnO_3$. *Phys. Rev. B* **1998**, *57*, R3189–R3192.

(19) Mellan, T. A.; Corà, F.; Grau-Crespo, R.; Ismail-Beigi, S. Importance of Anisotropic Coulomb Interaction in $LaMnO_3$. *Phys. Rev. B* **2015**, *92*, 085151.

(20) Franchini, C.; Kovacik, R.; Marsman, M.; Murthy, S. S.; He, J.; Ederer, C.; Kresse, G. Maximally Localized Wannier Functions in $LaMnO_3$ within PBE + U, Hybrid Functionals and Partially Self-Consistent GW: An Efficient Route to Construct ab initio Tight-Binding Parameters for e_g Perovskites. *J. Phys. Condens. Matter* **2012**, *24*, 235602.

(21) Stavitski, E.; de Groot, F. M. The CTM4XAS Program for EELS and XAS Spectral Shape Analysis of Transition Metal L Edges. *Micron* **2010**, *41*, 687 – 694.

(22) Castleton, C. W. M.; Altarelli, M. Orbital Ordering in the Manganites: Resonant x-ray Scattering Predictions at the Manganese L_{II} and L_{III} Edges. *Phys. Rev. B* **2000**, *62*, 1033–1038.

(23) Orgiani, P.; Galdi, A.; Aruta, C.; Cataudella, V.; De Filippis, G.; Perroni, C. A.; Marigliano Ramaglia, V.; Ciancio, R.; Brookes, N. B.; Moretti Sala, M.; Ghiringhelli, G.; Maritato, L. Multiple Double-Exchange Mechanism by Mn^{2+} Doping in Manganite Compounds. *Phys. Rev. B* **2010**, *82*, 205122.

(24) Dovesi, R. et al. CRYSTAL17 User's Manual. Universita di Torino, Torino, 2017.

(25) http://www.crystal.unito.it/Basis_Sets/Ptable.html.

(26) Muñoz, D.; Harrison, N. M.; Illas, F. Electronic and Magnetic Structure of $LaMnO_3$ from Hybrid Periodic Density-Functional Theory. *Phys. Rev. B* **2004**, *69*, 085115.

(27) Muscat, J.; Wander, A.; Harrison, N. On the Prediction of Band Gaps from Hybrid Functional Theory. *Chem. Phys. Lett.* **2001**, *342*, 397 – 401.

(28) Mallia, G.; Orlando, R.; Llunell, M.; Dovesi, R. In *Computational Materials Science*; Catlow, C., Kotomin, E., Eds.; Nato Sci. SER. III: Comp. Syst. Sci.; IOS Press, Amsterdam, 2003; Vol. 187; pp 102–121.

(29) Cora, F.; Alfredsson, M.; Mallia, G.; Middlemiss, D. S.; Mackrodt, W. C.; Dovesi, R.; Orlando, R. In *Principles and Applications of Density Functional Theory in Inorganic Chemistry II*; Kaltsoyannis, N., McGrady, J., Eds.; Structure & Bonding; Springer Berlin / Heidelberg, 2004; Vol. 113; pp 171–232.

(30) Goodenough, J. B. Perspective on Engineering Transition-Metal Oxides. *Chem. Mater.* **2013**, *26*, 820–829.

(31) Garvie, L.; Craven, A. J. High-Resolution Parallel Electron-Energy-Loss Spectroscopy of Mn L(2,3)-Edges in Inorganic Manganese Compounds. *Phys. Chem. Miner.* **1994**, *21*, 191–206.

(32) Orgiani, P.; Galdi, A.; Aruta, C.; Cataudella, V.; De Filippis, G.; Perroni, C. A.; Marigliano Ramaglia, V.; Ciancio, R.; Brookes, N. B.; Moretti Sala, M.; Ghir-

inghelli, G.; Maritato, L. Multiple Double-Exchange Mechanism by Mn_{2+} Doping in Manganite Compounds. *Phys. Rev. B* **2010**, *82*, 205122.

(33) Ahmad, E. A.; Tileli, V.; Kramer, D.; Mallia, G.; Stoerzinger, K. A.; Shao-Horn, Y.; Kucernak, A. R.; Harrison, N. M. Optimizing Oxygen Reduction Catalyst Morphologies from First Principles. *J. Phys. Chem. C* **2015**, *119*, 16804–16810.

(34) Zhu, Y.; Zhou, W.; Yu, J.; Chen, Y.; Liu, M.; Shao, Z. Enhancing Electrocatalytic Activity of Perovskite Oxides by Tuning Cation Deficiency for Oxygen Reduction and Evolution Reactions. *Chem. Mater.* **2016**, *28*, 1691–1697.

(35) Calle-Vallejo, F.; Inoglu, N. G.; Su, H.-Y.; Martínez, J. I.; Man, I. C.; Koper, M. T. M.; Kitchin, J. R.; Rossmeisl, J. Number of Outer Electrons as Descriptor for Adsorption Processes on Transition Metals and their Oxides. *Chem. Sci.* **2013**, *4*, 1245–1249.

(36) Cho, D.-Y.; Oh, S. J.; Kim, D. G.; Tanaka, A.; Park, J. H. Investigation of Local Symmetry Effects on the Electronic Structure of Manganites: Hexagonal $YMnO_3$ versus Orthorhombic $LaMnO_3$. *Phys. Rev B* **2009**, *79*, 415.

TOC Graphic

